FULL PAPER

Source constraints for the 2015 phreatic eruption of Hakone volcano, Japan, based on geological analysis and resistivity structure

Kazutaka Mannen[1]*, Toshikazu Tanada[2], Akira Jomori[3], Takashi Akatsuka[4], George Kikugawa[1], Yui Fukazawa[5], Hiroyuki Yamashita[6] and Koichiro Fujimoto[5]

Abstract

On June 29, 2015, a small phreatic eruption occurred in the most intensively steaming area of Hakone volcano, Japan. A previous magnetotelluric survey for the whole volcano revealed that the eruption center area (ECA) was located near the apex of a bell-shaped conductive body (resistivity < 10 Ωm) beneath the volcano. We performed local, high-resolution magnetotelluric surveys focusing on the ECA before and after the eruption. The results from these, combined with our geological analysis of samples obtained from a steam well (500 m deep) in the ECA, revealed that the conductive body contained smectite. Beneath the ECA, however, the conductive body intercalated a very local resistive body located at a depth of approximately 150 m. This resistive body is considered a vapor pocket. For the 2 months prior to eruption, a highly localized uplift of the ECA had been observed via satellite InSAR. The calculated depth of the inflation source was coincident with that of the vapor pocket, implying that enhanced vapor flux during the precursory unrest increased the porosity and vapor content in the vapor pocket. In fact, our magnetotelluric survey indicated that the vapor pocket became inflated after the eruption. The layer overlaying the vapor pocket was characterized by the formation of various altered minerals, and mineral precipitation within the veins and cracks in the layer was considered to have formed a self-sealing zone. From the mineral assemblage, we conclude that the product of the 2015 eruption originated from the self-sealing zone. The 2015 eruption is thus considered a rupture of the vapor pocket only 150 m below the surface. Even though the eruption appeared to have been triggered by the formation of a considerably deeper crack, as implied by the ground deformation, no geothermal fluid or rocks from significantly deeper than 150 m were erupted.

Keywords: Hakone volcano, Magnetotelluric surveys, CSAMT, Phreatic eruption, Sealing zone, Hydrothermal system, Fumarole, Resistivity structure

Introduction

A phreatic eruption results from the vaporization of fluids located at shallow depths beneath a volcano. Such vaporization is often triggered by the intrusion of magmatic fluid, which is sometimes detectable in well-monitored volcanoes (Yamaoka et al. 2016; Mannen et al. 2019). However, in many cases, there are long time lags between an intrusion of the magmatic fluid and the

subsequent phreatic eruption (Stix and De Moor 2018). Moreover, intrusions of magmatic fluid without a subsequent eruption are common. Thus, a "precursory" intrusion is frequently identified in hindsight after an eruption. This fact makes managing volcano alerts difficult because the sense of crisis and understanding of the reasons for restrictions around the volcano by local authorities diminishes as time advances after observable, yet subtle, volcanic unrest.

The time lag between an intrusion and eruption could be rooted in the underground structure of the volcano. A sealing zone, which is considered to form spontaneously

*Correspondence: mannen@onken.odawara.kanagawa.jp
[1] Hot Springs Research Institute of Kanagawa Prefecture, 586 Iriuda, Odawara, Kanagawa 250-0031, Japan
Full list of author information is available at the end of the article

Mannen *et al. Earth, Planets and Space* (2019) 71:135

Page 2 of 20

at the margin of a hydrothermal system, could be the key to understanding phreatic eruptions.

A sealing zone is a conceptual, yet widely accepted, structural element beneath an active volcano, and it can be formed at different depths from shallow to deep (Fournier 1999). A sealing zone near the surface is frequently called a cap rock. A cap rock is a clay-rich impervious zone formed by the hydrothermal alteration of the native rock or volcanic edifice. Because the clay that forms the zone is a highly conductive mineral called smectite, a cap rock has been recognized as a prominent conductive layer by magnetotelluric surveys on numerous volcanoes. The latest reports on such examples include the following volcanoes: Tateyama (Midagahara), Iwate, and Kuttara in Japan, and Furnas in the Azores (Aizawa et al. 2009; Goto and Johmori 2013; Seki et al. 2015, 2016; Hogg et al. 2018). Near the magma chamber, hydrothermal water in the crustal pores and fractures dissolves a large amount of silica and other solutes, which originate from the native rock and underlying degassing magma. This hydrothermal water occasionally migrates upward due to a change of stress or brittle failure and depressurization. These events result in the precipitation of silica and other minerals in the cracks and pores through which the fluid migrated (Weatherley and Henley 2013). A zone formed by the spontaneous closure of a porous system through the precipitation of minerals is called a self-sealing zone. The two aforementioned sealing zones form an important structure called a hydrothermal system, which encloses hydrothermal fluid between the surface and magma chamber, and hydrothermal fluid in the system is isolated from the peripheral ground water system. Within the hydrothermal system, the precipitation of minerals, hydrothermal alteration, and preexisting geological structures can form other sealing zones.

Although a sealing zone confines hydrothermal fluid, a phreatic eruption can occasionally occur. This suggests that the rupture of a sealing zone is a key element in a phreatic eruption. Thus, forecasting a phreatic eruption could be dependent upon the understanding and modeling of a sealing zone, especially the rupture process.

Hakone volcano had a minor phreatic eruption on June 29, 2015, that released a small volume of tephra (100 m^3) and small flux (< 1 m^3/s) of syn-eruptive mudflow, which outflowed directly from the vent (Mannen et al. 2018b). After the eruption, we performed an electromagnetic survey of the eruption center area. Because this area had been surveyed similarly before the eruption, we successfully detected a change in the distribution of the resistivity beneath the area of the eruption center. In this study, we also examined the borehole geology, eruption products, and surface water chemistry to interpret the resistivity structure before and after the eruption. Moreover,

we attempted to identify the sealing zone that controlled the 2015 eruption.

Geological and geophysical setting

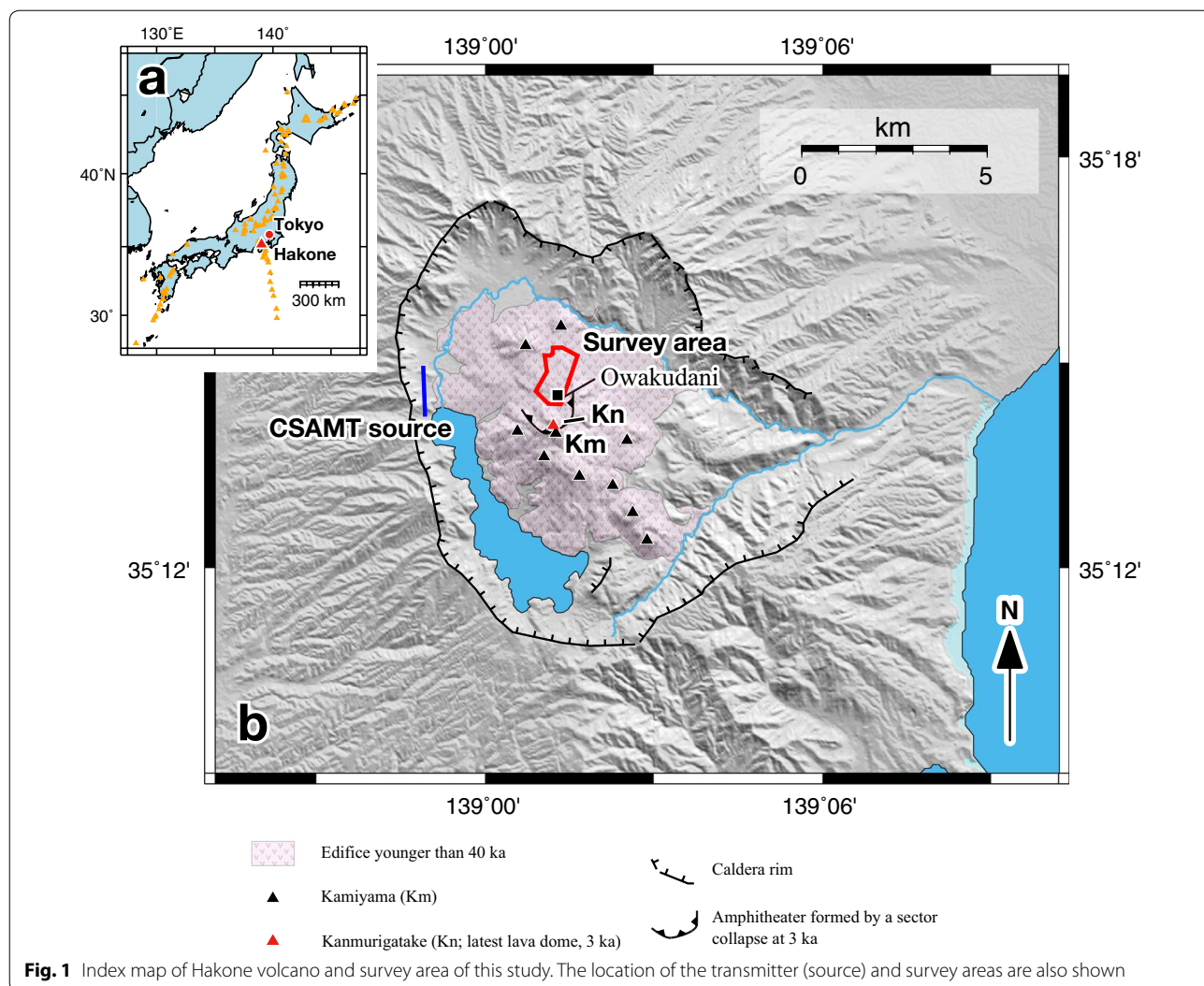### Hakone volcano and the Owakudani steaming area

Hakone volcano is an active volcano located approximately 100 km west of Tokyo, Japan. This volcano has a long eruptive history of more than 400 ka (The Geological Society of Japan 2007). During the history of this volcano, several catastrophic eruptions (with an estimated erupted volume of approximately 10 km^3) have occurred (230–40 ka), and a caldera with the dimensions of 11 km (N–S) × 8 km (E–W) has formed. From 40 ka to the present, the eruption centers of the volcano have been restricted within the central part of the caldera, and small andesitic stratovolcanoes and lava domes have formed. They are collectively called the "younger central cones."

The newest magmatic eruption, dated at 3 ka, occurred at the northernmost part of the younger central cones and formed a lava dome named Kanmurigatake. This eruption appears to have triggered a sector collapse of a preexisting stratovolcano named Kamiyama, and an amphitheater was formed. At the center of the amphitheater, Kanmurigatake formed, and the Owakudani steaming area is located on the eastern margin of the amphitheater (Fig. 1).

Owakudani is the largest actively steaming area of the volcano. The steaming area is divided by a ridge running from north to south. The eastern half of the steaming area forms a deep valley named Owakudani (meaning "great boiling valley"), which is also the name of this area. The Owakuzawa River flows at the bottom of the valley. At the head of the Owakudani Valley, hot springs have been artificially made by mixing steam from steam production wells (SPW) with water pumped up from the caldera floor. The deepest SPW, known as No. 52 (hereafter, SPW52), is 500 m deep, and the elevation of its well mouth is 998 m above sea level (asl). In this study, cuttings retrieved during the drilling of SPW52 were examined to reveal the subsurface geology of the steaming area. In a previous study, steam emitted from SPW52 was called "B gas," and its chemistry was monitored (Ohba et al. 2011).

The 2015 eruption occurred in the eastern half of the Owakudani steaming area and formed new craters and fumaroles that are located within a radius of approximately 100 m around SPW52 (Doke et al. 2018; Mannen et al. 2018b). In this study, we refer to this location as the eruption center area (ECA).

The western half of the Owakudani area formed patchy bare fumarole areas within a forest. Because this area is open to the public, it is called Enchi (picnic area). The Enchi area remained unchanged after the eruption in

Mannen *et al. Earth, Planets and Space* (2019) 71:135

Page 3 of 20

Fig. 1 Index map of Hakone volcano and survey area of this study. The location of the transmitter (source) and survey areas are also shown

terms of fumarole temperature and intensity, although its Cl concentration, which is considered an indicator of the contribution of water from the hydrothermal system, has been gradually increasing in the spring waters of the area since the eruption (Mannen et al. 2018a, b).

Approximately 700 m north of the Owakudani area, there are several steaming areas that formed after the volcanic unrest of 2001 (Harada et al. 2012). These were named Regions A to E and were identifiable from aerial photos as areas where tall trees have died out (Fig. 2). Collectively, they are known as "Shin-funki" (new steaming). Among these, the activity of Regions A to D seems to have decreased, and shrubs have reappeared over the last several years. However, weak steaming rising from the surface continues to be visible, especially on winter days, and the subsurface temperature at a depth of 30 cm is greater than 90 °C in several parts of the area. Region E

is the largest and most active among the Shin-funki and is primarily soundless, yet intensive steaming continues to be visible, even on summer days.

The 2015 eruption

Because the 2015 eruption of Hakone volcano was described in detail in a previous study (Mannen et al. 2018b), only a summary is presented herein.

The 2015 eruption was preceded by deep, low frequency earthquakes and an increase in baseline length across the volcano, both of which are interpreted as signals of the replenishment of the magma chamber (> 10 km deep). In late April, a tectonic earthquake swarm with an epicenter shallower than several kilometers began. On May 3, a SPW (No. 39, 413 m deep) intensified to emit an unusual amount of steam. These observations typically indicate an increase in underground pressure. In fact, a satellite
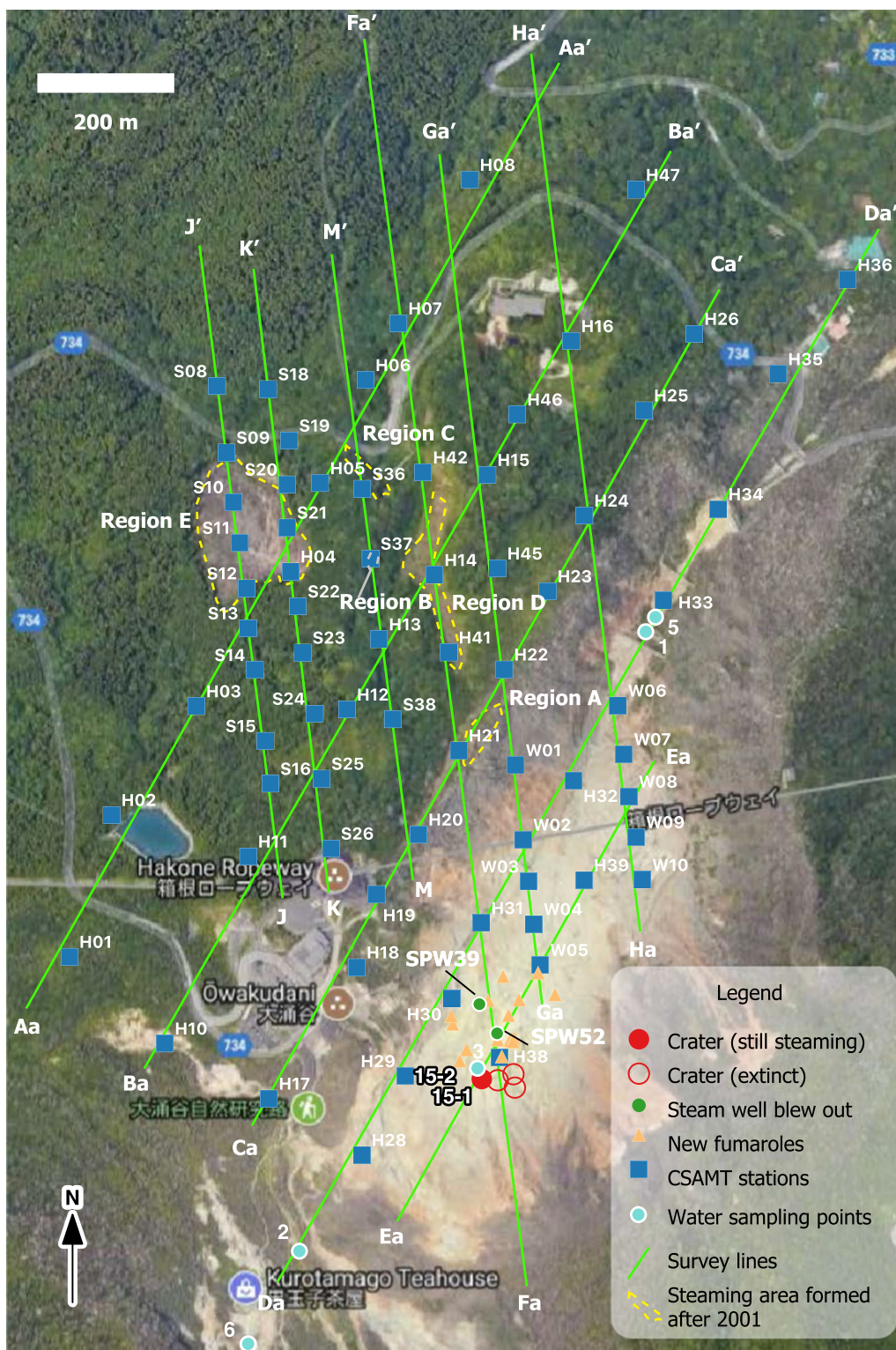
Fig. 2 Aerial photograph of study area with receiver stations and survey lines for 2D CSAMT analysis (photograph source: Google Earth). The center of the 2015 eruption is in the lower center of the map, and the craters and fumaroles formed by the eruption are shown. The locations of the steam production wells that blew out during the precursory unrest of the 2015 eruption and areas of newly formed fumaroles after 2001 are also depicted

Mannen *et al. Earth, Planets and Space* (2019) 71:135

Page 5 of 20

InSAR analysis detected a highly localized uplift around SPW52, which was attributed to an inflation beneath the well at a depth of approximately 100–150 m (Doke et al. 2018; Kobayashi et al. 2018). Hereafter, we called the inflation source a very shallow source (VSS). Inflations of the magma chamber and a hydrothermal system were also inferred after a detailed analysis of the Global Navigation Satellite System data (Harada et al. 2018). The seismic activity achieved a climax in mid-May and began to decrease; however, inflations of the VSS, magma chamber, and hydrothermal system continued without any rate changes (Doke et al. 2018; Harada et al. 2018).

On the morning of June 29 (Japan Standard Time in this study; JST = UTC + 9), an open crack formed beneath the Owakudani area, which was detected by tiltmeters and broadband seismometers (Honda et al. 2018). The formation of the open crack was also revealed by a satellite InSAR analysis. Its upper limit (830 or 854 m asl) and the strike direction (NW–SE) deduced by both analyses were consistent (Doke et al. 2018; Honda et al. 2018).

At virtually the same time as the crack formed, the beginning of a local uplift around SPW52 was observed by a ground-based InSAR, and pressurization immediately beneath the steaming area was indicated (Kuraoka et al. 2018). Because the visibility was poor on the day of the eruption, the timing of the onset of the eruption remains ambiguous; however, the beginning of gas emissions at 7:32, a mudflow or debris flow at approximately 11:00, and ash fall at approximately 12:30 were assumed from different observations (Mannen et al. 2018b; Yukutake et al. 2018).

The eruption continued until the morning of July 1, when the largest tremor activity was observed (Yukutake et al. 2017). After the eruption, the inflation of the VSS ceased; however, inflations of the hydrothermal system and magma chamber continued without a significant rate change until the end of August (Doke et al. 2018; Harada et al. 2018). Steaming from the newly formed crater and fumaroles has continued to the present. Temperatures of the steam exceed 160 °C in the ECA (Mannen et al. 2018a), while the temperature of the fumaroles in the Enchi area remains less than the local boiling point, as it was before the eruption (approximately 97 °C).

Previous magnetotelluric surveys

In 2018, we conducted a controlled source audio frequency magnetotelluric (CSAMT) survey (Sandberg and Hohmann 1982), which revealed the resistivity structure beneath the ECA and adjacent area north of it (Fig. 2). Fortunately, in this area, with dimensions of approximately 1000 m × 700 m, the Kanagawa Prefectural Government also conducted CSAMT surveys in 2008, 2013, and 2014. Although the number of receiver sites changed moderately depending on the year, the survey method, transmitter sites, and receiver sites were the same as the previous surveys and our 2018 survey. Thus, we could compare the resistivity structures before and after the eruption. The details of the data acquisition in the field and data processing in the laboratory are described in the "CSAMT survey" section.

From the previous CSAMT surveys, Mannen et al. (2018b) showed a representative resistivity cross section obtained in the 2014 survey and demonstrated the existence of a plate-like conductive body beneath the study area. The top of the plate-like conductive body reached the surface in the southernmost part of the study area, where the Owakudani steaming area is located, and dipped toward the north. In the 2014 survey, a small conductive body was also identified, which branched upward to meet the ground surface from the plate-like conductive body. Because the branched conductor was located beneath a newly formed steaming area (Region E), the branch and main conductive body were considered to represent routes of hydrothermal fluid migrating from depth (Mannen et al. 2018b). Unfortunately, the ECA was not covered by the surveys in 2013 and 2014. Because this study focused on the resistivity structure beneath the ECA, the surveys conducted in 2008 and our 2018 survey were mainly analyzed.

In addition to the CSAMT analysis mentioned above, Yoshimura et al. (2018) conducted extensive audio frequency magnetotelluric surveys of Hakone volcano in 2011 and 2013, and they revealed that there was a three-dimensional resistivity structure of 14 km (E–W) × 20 km (N–S) and up to 5 km in depth. The inversion results revealed two massive conductive areas. One of them was interpreted to be caldera structures buried beneath the morphology of the caldera floor around the younger central cones. In the central part of the caldera, another conductive (< 10 Ωm) structure was found. The conductive structure was bell shaped, the top of which was located immediately beneath the Owakudani area. Yoshimura et al. (2018) interpreted the bell-shaped conductor and the resistive body inside it as a clay-rich cap rock and a hydrothermal reservoir, respectively.

Temperature profile of SPW52

We do not have direct information regarding the geothermal structure of SPW52 because logging for it has not yet been implemented. Ohba et al. (2011) repeatedly measured the temperature of the steam from SPW52 from 2001 to 2009. It ranged from 132 to 163 °C, corresponding to 2741–2802 kJ/kg of enthalpy, assuming no liquid was contained at the well mouth (0.1 MPa). Assuming hydrostatic pressure and isoenthalpic decompression of the steam from the well bottom to the surface, Ohba et al.

Mannen *et al. Earth, Planets and Space*   (2019) 71:135

Page 6 of 20

(2011) calculated the temperature at the bottom of the well bottom to be 262 °C. The steam table suggested that the steam in SPW52 is dry throughout the well when the steam temperature at the surface is greater than 163 °C.

Data

Geological samples

To understand the subsurface geology of the ECA, we examined cuttings from SPW52. The well was drilled in 1995, and the cuttings were collected every 10 m to a depth of 470 m. Furthermore, we examined the mudflow deposit that flowed directly out of the vent during the 2015 eruption. We sampled the mudflow deposit at Location 5 and other points downstream of the river (Fig. 2). In this study, we observed thin sections and hand specimens; we conducted X-ray diffraction (XRD) analysis and chemical analysis of these geological samples.

XRD data were obtained using an Ultima-IV (Rigaku Co. Ltd.) installed at Tokyo Gakugei University, and peaks in the obtained diffraction pattern were identified using JADE 6 software (Material Data, Inc). To identify the clay minerals, ethylene glycol saturation and HCl treatment protocols were applied to the oriented samples.

A chemical analysis of the samples was performed using an X-ray fluorescence analyzer. The analyzer was a Rigaku ZSX Primus II located at the Kanagawa Prefectural Museum of Natural History. Because heating samples in a crucible generates SO_2, it was expected that the samples would have a high sulfur content. This meant that the glass bead method, which is a standard method for high precision analysis, was inapplicable in this case. We, therefore, adopted the fundamental parameter method, which was preinstalled on the analyzer, for the pressed powder samples.

We could not sample the ash fall because it was thin, making it difficult to gather the required amount; however, Yaguchi et al. (2019) successfully acquired pyroclastic fall from the 2015 eruption and reported the bulk rock chemistry and mineral assemblage of the deposit. Their results are discussed with our data.

Water resistivity

Because the resistivity of the Earth is controlled not only by that of the bulk rock, but also by the porosity and chemistry of the interstitial water, it was important to have water resistivity data for the study area. Since our entry to the area was permitted in 2016, we have routinely monitored the water quality in the Owakudani area, including spring water, river water, and water from bubbling mud hells. Water resistivity was measured on sampling days using a conductivity meter (DS15, Horiba) at the Hot Springs Research Institute of Kanagawa Prefecture.

CSAMT survey

In this study, we used a "scalar CSAMT" methodology (Zonge and Hughes 1991). In this method, a transmitter injects electrical current into the ground at near audio frequencies via grounded dipole sources, while a receiver records the electric field parallel to the dipole source and the magnetic field perpendicular to the dipole (Johmori et al. 2010; Goto and Johmori 2013). The survey was conducted from March 6–23, 2018. The configuration of our CSAMT survey included transmitter and receiver sites, injecting an electrical current and frequencies, analysis, and a two-dimensional (2D) inversion technique. This configuration was the same as that of previous surveys planned by the Kanagawa Prefectural Government in 2008, 2013, and 2014, which were conducted by two authors of this paper (AJ and TA); the resolution of the analogue–digital conversion was improved in 2018 to 24-bit from 16-bit in the previous surveys.

The transmitter source was set approximately 3–4 km west of the survey area (Fig. 2). At the transmitter source (=dipole source), a cable 1.4 km in length was set in a near N–S direction, and 50 electrodes (each approximately 60 cm long) were grounded at each end of the cable. The survey area was a N–S trending quasi-rectangular area (Fig. 2). Within the area, we took measurements at 72 sites, along six NS trending lines and five NNE–SSW-trending lines. In this study, 23 frequencies of electrical current (5.0 A maximum) were injected into the ground in two sets. These frequencies ranged from 1 to 8192 Hz in the first set and from 20 to 5120 Hz in the second set; they were doubled with each injection (1, 2, 4, 8, 16, 32, 64, 128, 256, 512, 1024, 2048, 4096, 8192 and 20, 40, 80, 160, 320, 640, 1280, 2560, 5120 Hz, respectively).

The real and imaginary parts of the CSAMT data were processed using Fourier transform for each frequency. After applying an enhancement process to the data using a stacking approach to improve the signal-to-noise ratio, the apparent resistivity (ρ_a) and phase angles (ϕ) of the electric and magnetic fields were calculated from the measured electric and magnetic field using the following equations:

$$\rho_a = \frac{1}{2\pi f \mu_0} \left| \frac{E}{H} \right|^2,$$

$$\phi = \phi_E - \phi_H,$$

where f is the frequency, μ_0 is the magnetic permeability ($4\pi \times 10^{-7}$ H/m), E is the intensity of the electric field (V/m), and H is the intensity of the magnetic field (A/m). ϕ_E and ϕ_H are the observed phases of the electric and magnetic fields, respectively.

Mannen *et al. Earth, Planets and Space*   (2019) 71:135

Page 7 of 20

In the survey, CSAMT data were assumed to have been measured mainly in a far-field region because the skin depth was small due to the low resistivity of the survey area (1–10 Ωm). At eleven of the survey stations, there were possible minor influences of the near-field effect on the CSAMT data (frequency of 1 Hz). However, the number of such stations and possible near-field effects were considered to be limited; hence, the near-field effect in this survey was considered to have no significant influence on the modeling of the resistivity structure. The maximum penetration depth of the survey was estimated to be approximately 500 m based on the average resistivity of the study area (1–10 Ωm) and the distance from the source to the observation stations (3–4 km).

To evaluate the quality of the observed data, a one-dimensional inversion was also applied; however, in this study, the final resistivity cross sections were obtained using 2D inversion code developed by Sasaki (1986). The 2D inversions were performed along survey lines that were parallel to the transmitter source using transverse magnetic (TM) mode software. The mesh size of the finite element was 15 m for the horizontal axis and 6–20 m for the vertical axis. Each inversion block (i.e., the unit used to calculate the resistivity by 2D inversion) consisted of four meshes–two vertically and two horizontally neighboring meshes. The resistivity of each inversion block was calculated using a nonlinear least squares method, and the calculation was iterated eight times.

The initial resistivity was set to 2 Ωm and 20 Ωm. Although 20 Ωm was found to have better convergence, both initial frequencies provided similar resistivity structures up to a certain depth. The depth was defined as the maximum depth of penetration, and the resistivity structure beneath it was masked in the resistivity cross sections displayed later.

The root mean square residual (RMSR), which is a metric for solution convergence, is defined as:

$$\mathrm{RMSR} = \left\{ \frac{\sum_{i=1}^{n} (\ln(\rho_{\mathrm{af}}) - \ln(\rho_{\mathrm{ac}}))^2}{n} \right\}^{0.5},$$

where n is the number of data ($=$ number of survey frequency $\times$ number of receiver points), ρ_{af} is the observed apparent resistivity, and ρ_{ac} is the calculated apparent resistivity after 2D inversion. The RMSR of the survey lines in this study ranged from 0.062 to 0.134.

Results

Geology of SPW52 and the 2015 eruption products
The mineral assemblage obtained from the XRD analysis is presented in Table 1. Based on the mineral assemblage and lithology, we subdivided the borehole geology into four layers, named Layers A to D, in descending order.

Layer A (998–888 m asl) characteristically contained visible pyrite and gypsum. It was noteworthy that this layer had various minerals, including calcite and alunite, which were absent in the other layers. Layer B (878–628 m asl) was rich in quartz. Layer C (618–558 m asl) was characterized as a layer where illite and chlorite were the dominant clay minerals instead of smectite, which was dominant in Layers A and B. Layer D (548–528 m asl) was characterized by the coexistence of smectite and chlorite.

Because the cuttings obtained from the SPW52 were highly altered, it was difficult to deduce the original rock based only on the microscopic and macroscopic textures. However, the cuttings of Layers A and B demonstrated a variety of color and grain size, whereas Layers C and D were monotonous in color and grain size. This observation signified that Layers A and B were polymictic, while Layers C and D were monomictic. Because the geology of this area was formed by breccia (talus and debris avalanches) and lavas, the original rocks of Layers A and B were assumed to be breccia, and Layers C and D were assumed to be lavas.

The mineral assemblage of the eruption products is displayed in Table 2. The solid content of the mudflow and ash fall deposits (Yaguchi et al. 2019) contained a variety of minerals, including cristobalite, plagioclase, gypsum, alunite, and pyrite, and smectite was the dominant clay mineral. This mineral assemblage of smectite as the dominant clay mineral with various minerals was similar to that of Layer A.

Whole rock chemistry of SPW52 and the 2015 eruption products
The bulk rock chemistry of the samples from SPW52 and products of the 2015 eruption, such as the mudflow deposit and ash fall (Yaguchi et al. 2019), is listed in Table 3. The content of each element was displayed as its oxide concentration was normalized by concentration (wt %) of Al_2O_3, which is considered to be the most immobile element during hydrothermal alteration. This normalization helps to discriminate addition and removal of cations during the hydrothermal alteration. Our chemical analysis of the cutting samples from SPW52 indicated no significant variation through the entire depth of the well for Ti and Fe (Fig. 3a); however, Si, Ca, Mg, Na, K, and S appeared to vary among the layers (Fig. 3b–d).

Among these elements, the Na content showed a significant difference in the sections and formed two groups: high (> 0.14) for the deep sections (≤ 858 m asl) and low (< 0.12) for the shallow sections (≥ 868 m asl) (Fig. 3b). The range of Na concentrations of the groups was also different, as it was narrow for deep sections (0.19–0.14)

Mannen *et al. Earth, Planets and Space* (2019) 71:135

Page 8 of 20

Table 1 Abundance of altered minerals in SPW52 cuttings

Dep. (m)	Level (m asl)	Mineral abundance[a]													Layer[b]
		Cr	Tr	Qz	Sm	Il	Ch	Pl	Gy	Ah	Al	Py	Mg	Ca	
10	988	3			2			5	3						A
20	978	4			4			3	3						A
30	968	3			3			3	5						A
40	958		3					2	5		3	2			A
50	948	4			4			3	3		3	3		5	A
60	938	3		2	4			5	3		2	3			A
70	928	3		4	4			5	2			3			A
80	918	3			4			5	3			3			A
90	908				1			5	2		3				A
100	898			5				3	2		2				A
110	888			3	3			5	1		1				A
120	878			3	3			5	2						B
130	868			3	3			5	3						B
140	858	2		2	3			5		3					B
150	848	3		5	3			3		2					B
160	838	2		5			3	3							B
170	828	3		5	3			4		2					B
180	818	3		5	3			3							B
190	808	2		5	3			3							B
200	798	3		5	3			3							B
210	788	3	4	5	3			4							B
220	778	3	3	3	4			5					2		B
230	768	3		5	4			4							B
240	758	3		4	4			5							B
250	748			5	3			4							B
260	738	3		5	3			3							B
270	728	2		5	3			3				4			B
280	718	3		5	3			4							B
290	708			3	2			5							B
300	698	3		5	3			4							B
310	688	3		5	3			4							B
320	678	2		5				3							B
330	668	2		4	3			5							B
340	658	3		3	3			5							B
350	648	2		5	3			3				2			B
360	638	2		5	2			3				2			B
370	628	3		5	3		3	3				3			B
380	618	3		5		3	3	4				3			C
390	608	3		5		3	3	3				2			C
400	598	3		3		3	3	5				2	2		C
410	588	3		4		2	3	5				1			C
420	578	3		5		3	3	4				3			C
430	568	2		5		2	3	4							C
440	558			5		2	3	3					3		C
450	548			5	3			4					2		D
460	538	4		5	3		3	4							D
470	528	3		5	3	3	3	4							D

Cr cristobalite, *Tr* tridymite, *Qz* quartz, *Sm* smectite, *Il* illite, *Ch* chlorite, *Pl* plagioclase, *Gy* gypsum, *Ah* anhydrite, *Al* alunite, *Py* pylite, *Mg* magnetite, *Ca* calcite

[a] Abundance is defined by peak intensity. 5, maximum intensity (MI); 4, > 50% of MI; 3, ≥ 10% of MI; 2, ≥ 5% of MI; 1, < 5% of MI

[b] Layers defined by mineral assemblage. See text

Table 2 Abundance of altered minerals in the product of the 2015 eruption

Code	Level	Mineral abundance[a]										
		Cr	Tr	Qz	Sm	Il	Ch	Pl	Gy	Ah	Al	Py
150629-1	Syn-eruptive mud flow (river bank deposit)	3						5	3		2	2
150629-2	Syn-eruptive mud flow (suspension in water)	2							5		2	2
150630	River bank deposit	3			3			5	3		3	3
**	Ash fall deposit	○	○	○	○			○	○	○		○

[a] See Table 1 for abbreviation and definition of abundance. ○ indicates detected. ** Yaguchi et al. (2019). No relative abundance is shown

and wide for shallow sections (0.11–0.02). This trend of high concentrations and small deviations in deep sections, and low concentrations and large deviations in shallow sections was also observed for Si, Ca, Mg, and K. However, the trend was less significant than that of Na; certain samples from the shallow group demonstrated concentrations as high as that of the deep group. The concentration of S suggested the opposite trend of these elements in terms of concentration with low concentrations and small deviation at deep levels and high concentrations and large deviation at shallower levels (Fig. 3d). It was noteworthy that the boundary depth of the deep and shallow groups (approximately 860 m asl) was slightly deeper than the petrographical boundary between Layers A and B (approximately 880 m asl).

The 2015 eruption products (i.e., the mudflow and ash fall deposits) indicated reduced concentrations for Si, Ca, Mg, Na, and K and a higher concentration for S (Fig. 3). This trend indicated by the 2015 eruption product is similar to that of Layer A.

Water resistivity

The resistivity of the surface and hot spring waters in the Owakudani area is displayed in Additional file 1 and is summarized in Fig. 4. Surface water, such as river and spring waters, demonstrated relatively high resistivity (2–4 Ωm). Mud hell water, which was common in the Owakudani steaming area even before the eruption, also indicated relatively high resistivity (predominantly 0.7–2 Ωm). The moderately conductive nature of the mud hell water could be attributed to a higher concentration of sulfate ions, added by low-temperature fumaroles (approximately 97 °C; boiling point on the ground surface), which contained SO_2.

Conversely, water from the crater pond that formed shortly after the eruption and persisted more than a year revealed significantly lower resistivity (0.03–0.5 Ωm). Moreover, a mud hell developed near a fumarole that was newly formed during the 2015 eruption demonstrated similar values (0.07–0.4 Ωm). The fumaroles had high temperatures (> 130 °C), and waters in them seemed to be strongly influenced by the high-temperature fumarole gas, which contained a large amount of SO_2 and HCl.

These facts indicated that the surface waters have relatively high resistivity values, even in the fumarole area; however, significant conductive waters exist locally near the route of the high-temperature volcanic gas ascending from depth.

Resistivity structure of the study area

The resistivity cross sections obtained for the different survey lines, from both the present and previous study data, are presented in Additional file 2. Because the following discussion focuses on the subsurface structure of the ECA, here we show the resistivity cross section across the ECA along a survey line, Fa (Fig. 5). Moreover, to evaluate the validity of the 2D inversion of the survey line, Fa, the observed and inverted resistivity as a function of the site and frequency are displayed in Fig. 6. Examples of the raw data, apparent resistivity, and phase angle obtained in the 2008 and 2018 surveys are displayed in Fig. 7.

In Fig. 5, three layers (resistive body at the top, conductor body in the middle, and resistive body in the bottom of the survey range) are recognizable. Utilizing the definition of Yoshimura et al. (2018), we set the boundary value of the resistivity at 10 Ωm and subdivided the resistivity structure into Layers I to III in descending order.

Layer I was a resistive layer (> 10 Ωm) near the surface, although it was absent or nearly absent near the ECA and beneath the survey lines along the Owakudani Valley (survey lines E and D); however, it became thicker (> 200 m) in the northern part of the study area. Because the area where Layer I occurred is covered by dense forest and its subsoil geology was assumed to be mainly fresh lavas and volcaniclastics, we interpreted Layer I as fresh volcanic sediments.

Layer II was a conductive layer (< 10 Ωm) beneath Layer I. It surfaced in the steaming area and at the bottom of the Owakudani Valley (survey lines E and D).

Table 3 Bulk rock chemistry of cutting samples from SPW52 and products of the 2015 eruption

Depth/sample	Elevation	SiO_2^a	TiO_2^a	$Fe_2O_3^a$	MgO^a	MnO^a	CaO^a	Na_2O^a	K_2O^a	SO_3^a	$Al_2O_3^b$
SPW52											
10	988	2.68	0.040	0.335	0.101	0.005	0.233	0.080	0.026	0.335	20.645
20	978	3.13	0.041	0.372	0.202	0.003	0.217	0.029	0.014	0.630	17.731
30	968	2.95	0.040	0.393	0.100	0.001	0.267	0.029	0.021	1.134	16.808
40	958	3.17	0.044	0.434	0.054	0.000	0.450	0.051	0.015	1.832	14.138
50	948	3.20	0.040	0.329	0.115	0.001	0.248	0.058	0.019	0.947	16.759
60	938	3.63	0.046	0.391	0.348	0.005	0.609	0.097	0.024	0.525	14.943
70	928	3.27	0.044	0.345	0.332	0.004	0.282	0.093	0.030	0.493	16.935
80	918	3.56	0.046	0.399	0.469	0.003	0.360	0.111	0.023	0.396	15.660
90	908	2.08	0.035	0.371	0.007	0.000	0.155	0.022	0.004	1.415	19.585
100	898	2.76	0.042	0.411	0.009	0.000	0.217	0.057	0.014	1.611	16.302
110	888	2.86	0.036	0.315	0.177	0.002	0.317	0.060	0.016	0.985	17.304
120	878	2.99	0.040	0.322	0.333	0.005	0.306	0.058	0.014	0.862	16.831
130	868	2.99	0.041	0.407	0.180	0.002	0.324	0.091	0.017	1.168	16.047
140	858	3.44	0.040	0.385	0.317	0.009	0.386	0.153	0.016	0.402	16.250
150	848	3.45	0.039	0.354	0.261	0.006	0.395	0.163	0.024	0.423	16.331
160	838	3.32	0.039	0.347	0.274	0.006	0.341	0.141	0.019	0.576	16.463
170	828	3.43	0.038	0.365	0.274	0.000	0.377	0.141	0.017	0.600	15.970
180	818	3.33	0.040	0.354	0.256	0.005	0.353	0.145	0.020	0.556	16.473
190	808	3.31	0.041	0.349	0.259	0.006	0.375	0.166	0.026	0.471	16.617
200	798	3.32	0.041	0.363	0.258	0.006	0.365	0.163	0.025	0.486	16.567
210	788	3.33	0.038	0.348	0.248	0.006	0.364	0.161	0.025	0.584	16.374
220	778	3.58	0.038	0.394	0.331	0.008	0.415	0.178	0.031	0.116	16.392
230	768	3.49	0.039	0.373	0.292	0.007	0.401	0.188	0.033	0.104	16.832
240	758	3.36	0.037	0.359	0.293	0.007	0.419	0.181	0.031	0.078	17.307
250	748	3.31	0.041	0.355	0.305	0.007	0.395	0.186	0.032	0.195	17.117
260	738	3.33	0.040	0.354	0.327	0.009	0.419	0.176	0.028	0.348	16.548
270	728	3.28	0.039	0.340	0.293	0.007	0.412	0.183	0.026	0.345	16.838
280	718	3.41	0.040	0.350	0.283	0.007	0.381	0.182	0.032	0.187	16.990
290	708	3.35	0.039	0.341	0.309	0.008	0.413	0.175	0.030	0.309	16.695
300	698	3.43	0.039	0.361	0.353	0.011	0.427	0.164	0.023	0.370	16.150
310	688	3.33	0.039	0.361	0.335	0.010	0.434	0.161	0.022	0.340	16.533
320	678	3.38	0.044	0.349	0.371	0.012	0.436	0.159	0.023	0.545	15.800
330	668	3.43	0.041	0.359	0.341	0.010	0.422	0.161	0.022	0.377	16.192
340	658	3.45	0.041	0.361	0.354	0.011	0.423	0.160	0.021	0.405	16.012
350	648	3.42	0.041	0.363	0.340	0.011	0.448	0.168	0.024	0.399	16.051
360	638	3.47	0.039	0.404	0.443	0.010	0.619	0.156	0.024	0.327	15.372
370	628	3.48	0.044	0.416	0.441	0.011	0.644	0.158	0.025	0.330	15.230
380	618	3.40	0.038	0.386	0.423	0.010	0.557	0.161	0.026	0.344	15.712
390	608	3.39	0.041	0.392	0.443	0.010	0.527	0.145	0.024	0.332	15.824
400	598	3.28	0.043	0.376	0.426	0.009	0.472	0.141	0.027	0.403	16.151
410	588	3.24	0.044	0.384	0.401	0.009	0.460	0.148	0.030	0.352	16.445
420	578	3.30	0.043	0.387	0.399	0.010	0.505	0.146	0.029	0.357	16.155
430	568	3.38	0.044	0.397	0.346	0.010	0.484	0.172	0.036	0.123	16.662
440	558	3.28	0.043	0.407	0.381	0.010	0.457	0.174	0.032	0.139	16.832
450	548	3.28	0.047	0.418	0.398	0.011	0.454	0.161	0.034	0.088	16.932
460	538	3.24	0.042	0.391	0.419	0.010	0.420	0.158	0.031	0.193	16.913
470	528	3.28	0.047	0.426	0.397	0.011	0.470	0.151	0.033	0.109	16.833

Mannen *et al. Earth, Planets and Space*   (2019) 71:135

Page 11 of 20

Table 3 (continued)

Depth/sample	Elevation	SiO$_2^a$	TiO$_2^a$	Fe$_2$O$_3^a$	MgO^a	MnO^a	CaO^a	Na$_2$O^a	K$_2$O^a	SO$_3^a$	Al$_2$O$_3^b$
Mudflow deposit											
20150629-1		2.75	0.045	0.376	0.052	0.003	0.132	0.036	0.022	0.723	19.403
20150629-2		2.55	0.038	0.261	0.044	0.001	0.076	0.033	0.023	0.643	21.350
20150630		2.78	0.037	0.272	0.050	0.001	0.064	0.036	0.022	0.621	20.415

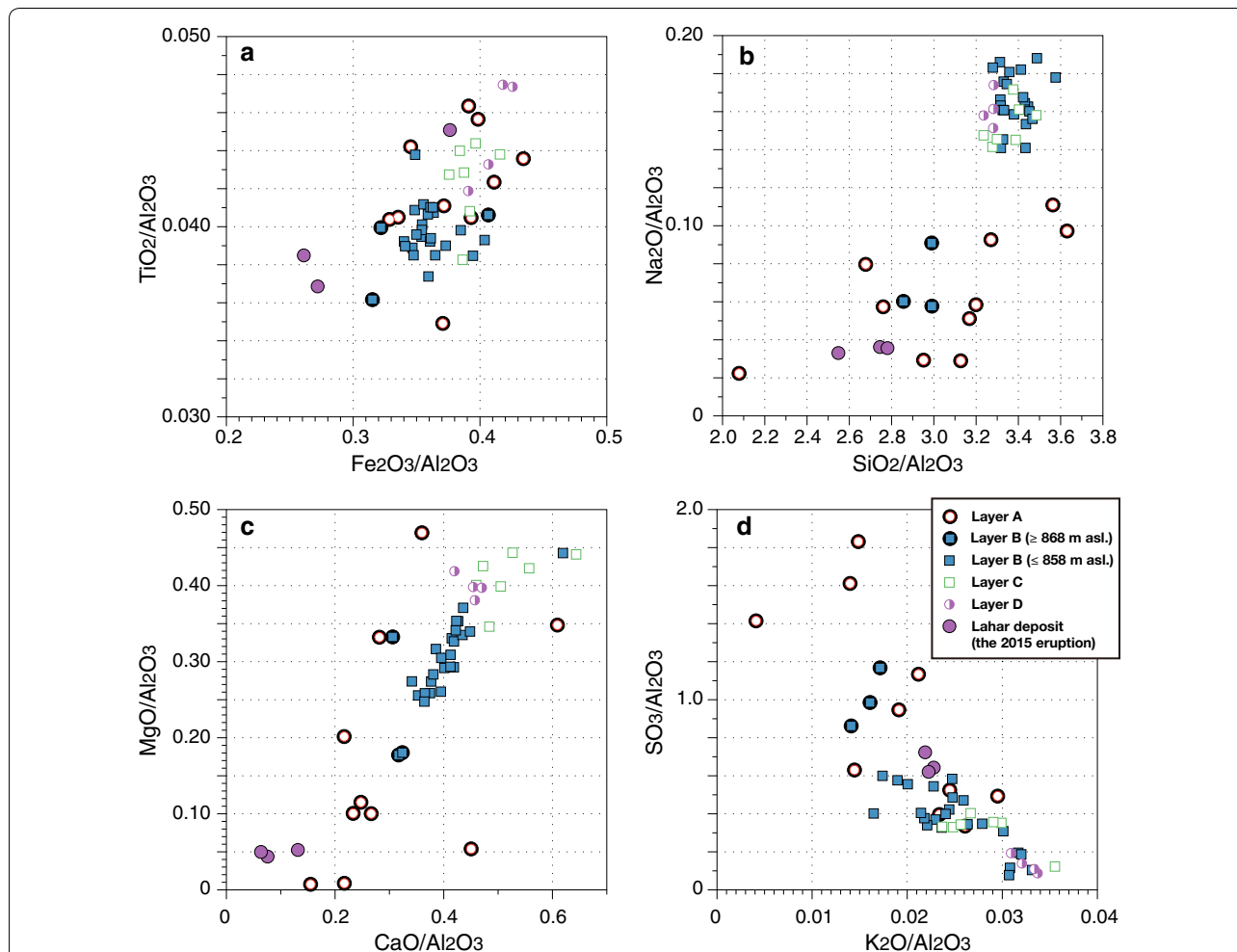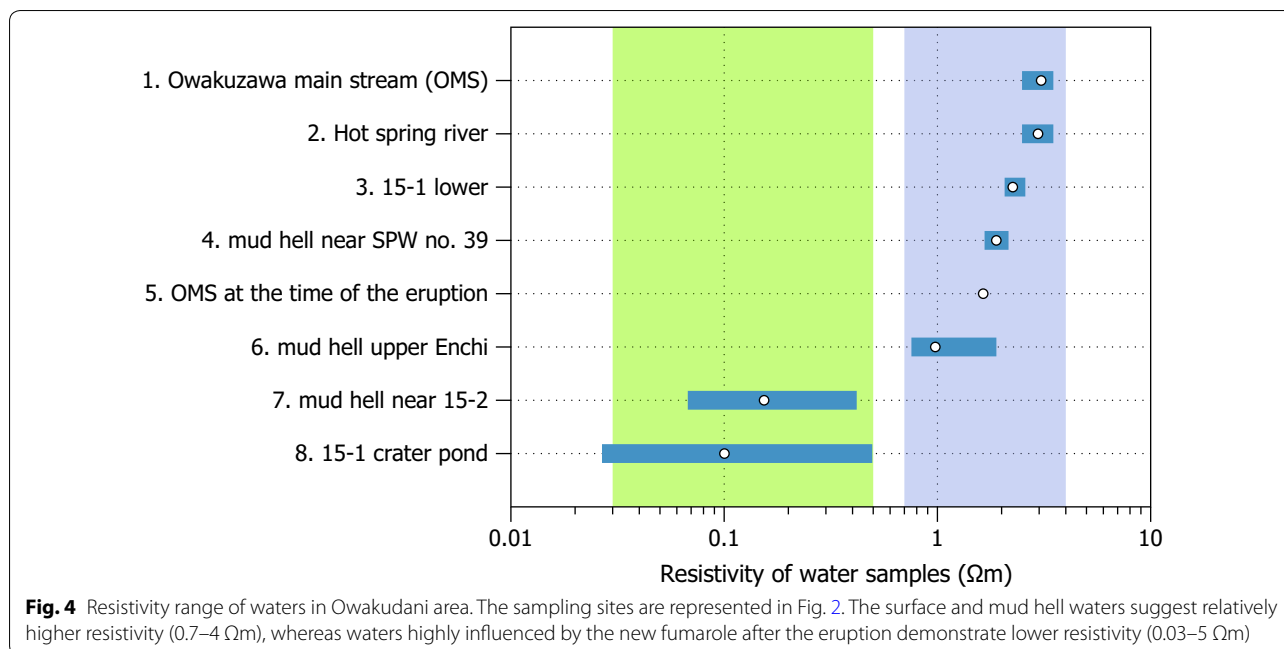^{a} Normalized by concentration of Al$_2$O$_3$ (wt%)

^{b} wt%

Fig. 3 Variation in rock chemistry of SPW52. To depict the modification of the chemical composition due to the hydrothermal alteration, all oxide contents are standardized using that of Al$_2$O$_3$, which is considered the most immobile element during hydrothermal alteration. The samples from deep depths (≤ 858 m asl) form a cluster, whereas those from shallower depths scatter, which indicates higher alteration at shallower depths. The deeper and shallower depths indicate no significant difference for the Fe and Ti content (**a**); however, lower Na, Si (**b**), Ca, Mg (**c**), and K (**d**) indicate leaching of those elements at shallow depths. The higher sulfur content in the shallow depths indicates that sulfuric acid is a leaching agent (**d**)

Because hydrothermally altered rocks were exposed in these areas, we interpreted Layer II as altered volcanic sediment. Layer II was found in all cross sections of this study, always dipping to the north (Additional file 2). This observation suggests that Layer II is a plate-like conductive body. In the northern part of the study area, the thickness of parts of Layer II is more than 300 m. However, in the southernmost part of the study area, Layer II intercalated a very local resistive body, and the thickness of Layer II above this was approximately 100 m (Fig. 5). Here, we define the resistive body as Region P.

Fig. 4 Resistivity range of waters in Owakudani area. The sampling sites are represented in Fig. 2. The surface and mud hell waters suggest relatively higher resistivity (0.7–4 Ωm), whereas waters highly influenced by the new fumarole after the eruption demonstrate lower resistivity (0.03–5 Ωm)

We consider the existence of Region P as highly probable because this body within Layer II was also recognized in the resistivity cross section of the baseline Ga, the station interval of which near the resistive body was short (approximately 50 m) (Additional file 2). Moreover, the raw data supported the existence of Region P. We included the raw data of the stations located immediately above Region P (H31 and H38) in Fig. 7b, c. The existence of Region P is indicated by the increase in apparent resistivity in the range from approximately 10 to 100 Hz. Region P was also implied from our preliminary forward calculation that used an imaginary cross section without Region P and is developed from Fig. 5a. The forward calculation indicated a resistivity that was significantly different from the observation.

In the northern part of survey line Fa, a conductive body that branched upward was observed and named Region U. We consider the existence of Region U as highly probable because the raw data from H07 also indicated a decrease in apparent density (Fig. 7a). Because weak steaming activity was observed near H07, Region U was considered to be a hot spring water upwelling from Layer II.

Layer III was the resistive layer (> 10 Ωm) beneath Layer II. Because this layer does not outcrop, we were not able to identify the geology that formed Layer III from the surface geological survey.

The three layers were also recognized in the 2008 and 2018 surveys. However, the thickness of Layer II from the 2018 survey was clearly thinner than that of 2008 (Fig. 5a). This thinning appears to have been caused by

an increase in resistivity at depth, which fits with the upward migration of the 10 Ωm contour. The increase in resistivity at depth was also suggested by the expansion of Region P (Fig. 5a, c).

Discussion
Resistivity structure and borehole geology
Yoshimura et al. (2018) identified a bell-shaped conductor (< 10 Ωm) beneath the central cone area and interpreted the conductor as a smectite-rich sealing zone, which confined a hydrothermal system within. However, because the resolution of the survey was not sufficient, the detailed dimensions and structure of the conductor remained uncertain. Owing to densely located stations, our CSAMT survey enabled us to obtain a local, yet high-resolution resistivity structure of Owakudani and its peripheral area and to locate Layer II, a plate-like conductive body beneath the study area. From the location, orientation, and resistivity values, we conclude that Layer II corresponds to the northern portion of the bell-shaped conductive body identified by Yoshimura et al. (2018).

To interpret the resistivity structure in a geological context, we extracted a vertical resistivity structure at the closest point to SPW52 from the 2D resistivity inversion along the survey line Fa. The resistivity structure obtained is displayed with the representative alteration minerals in Fig. 8. The boundary of the bulk rock chemistry (at approximately 860 m asl; Fig. 3) and the resistivity ranges of the surface water and water highly influenced by volcanic gas (Fig. 4) are also displayed in Fig. 8.
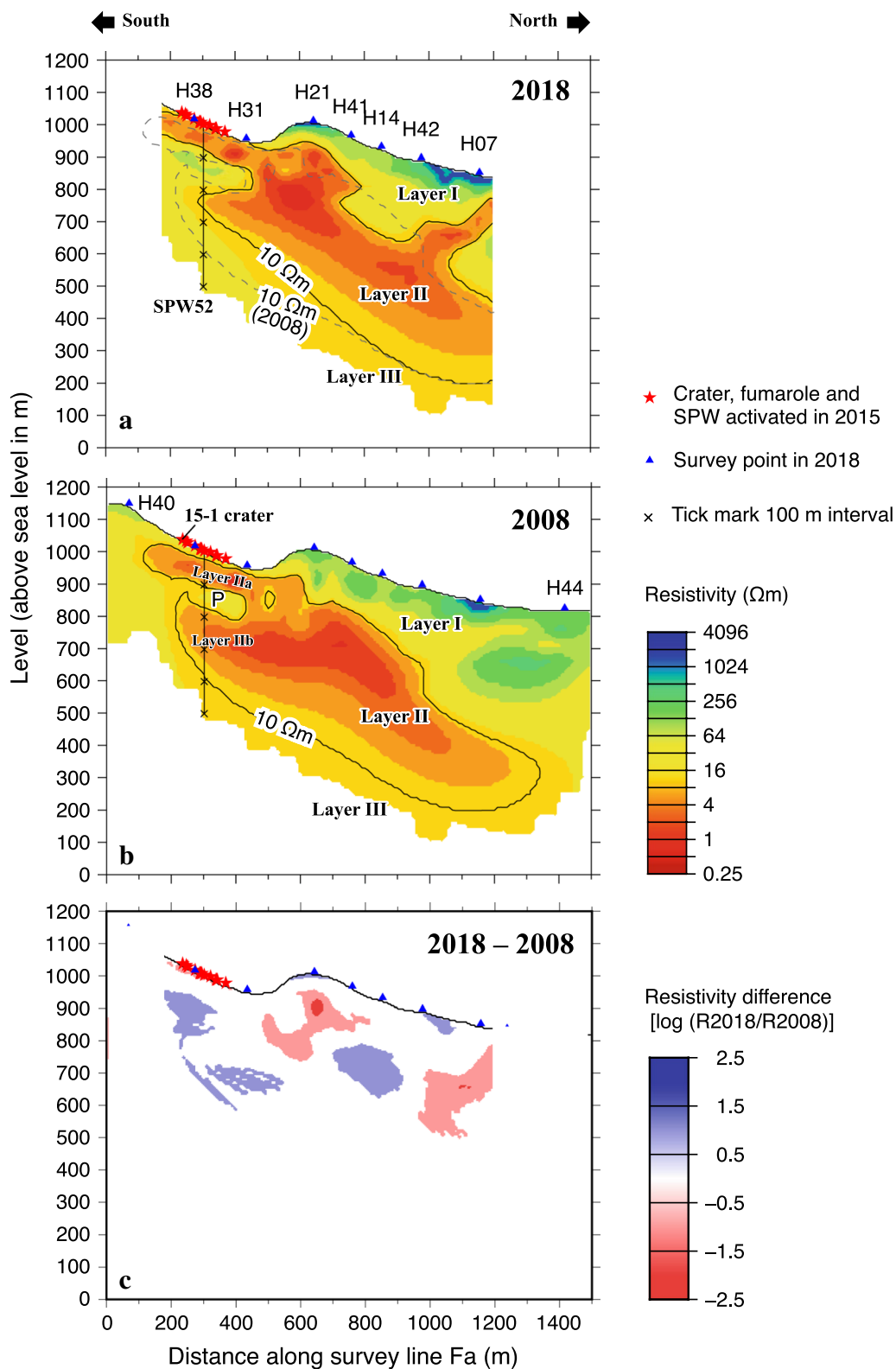
Fig. 5 Cross-sectional resistivity structure along survey line Fa: **a** 2018 survey, **b** 2008 survey, and **c** resistivity change in log (R2018–R2008). P indicates the resistive portion within Layer II, which is considered a vapor pocket. U indicates a possible upwelling of hot springs from Layer II. See text for a more detailed interpretation of P and U
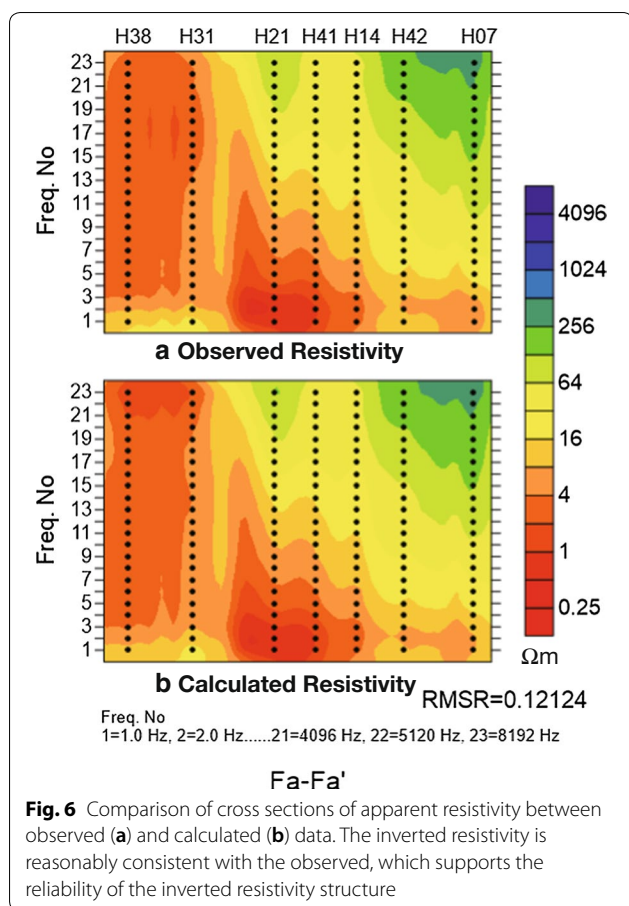
Mannen *et al. Earth, Planets and Space*   (2019) 71:135

Page 14 of 20

Fig. 6 Comparison of cross sections of apparent resistivity between observed (**a**) and calculated (**b**) data. The inverted resistivity is reasonably consistent with the observed, which supports the reliability of the inverted resistivity structure

Figure 8 shows that in 2008, the conductive (< 10 Ωm) zone ranged from near the surface to approximately 620 m asl, although a slightly resistive zone intercalated from 830–890 m asl, which was defined as Region P. Figure 8 also indicates that a smectite-rich layer ranged from approximately 620 m asl (lower boundary of Layer B) to the surface and that this range corresponded to the conductive zone. Thus, we conclude that Layer II, or the bell-shaped conductive body, is a smectite-rich zone as proposed by Yoshimura et al. (2018), although a pocket-like resistive zone intercalated. We will discuss the pocket-like resistive zone in the next section.

From the similarities of the location and resistivity values, we conclude that Layer III corresponds to the resistive body confined by the bell-shaped conductor and forms the hydrothermal system of the volcano (Yoshimura et al. 2018). Geologically, Layer III (< 620 m asl) corresponds to Layers C and D, which were found to contain illite and chlorite as the prevailing clay minerals instead of smectite. Experimental and field studies have revealed that in high temperatures, illite is more stable than smectite, and smectite–illite conversion occurs at approximately 200 °C (Hedenquist et al. 2000; Lee et al.

2010). However, the lack of pyrophyllite, anhydrite, and diaspore, which are altered minerals characteristically found at > 200 °C (Inoue 1995), indicates that the temperature in SPW52 would not significantly exceed 200 °C, even at the bottom of the well. From the steam temperature at the well mouth (132–163 °C), Ohba et al. (2011) calculated the temperature at the bottom of SPW52 as 262 °C, assuming hydrostatic pressure and isoenthalpic decompression of steam. However, we consider that such a high temperature at the bottom of SPW52 is unlikely, and vapor static pressure could be a more appropriate temperature profile of SPW52.

Significance of the Layer II structure beneath the ECA

In this section, we focus on the detailed resistive and geological structure within Layer II beneath the ECA and define Layers IIa and IIb, which form portions of Layer II above and below Region P (Fig. 5). Layer IIa ranges from the surface to a depth of approximately 110 m (890 m asl), which is virtually identical to Layer A. Layer A was rich in altered minerals, such as gypsum, alunite, calcite, and pyrite; most of these were found only in Layer A (Fig. 8). The altered mineral assemblage appears to be characteristic of a near-surface steam-heated zone of a geothermal system, where boiling, partition of dissolved gas, and possible oxidation occur (Henley and Ellis 1983). The formation of these minerals within the pores and cracks in the layer would reduce the permeability and form a self-sealing zone. In fact, formations of pyrite, which is easily degraded by oxygen-rich surface water, implies a low-permeability nature of Layer A. Calcite, which is easily dissolved by acidic water, appeared at 50 m deep, also indicating the low-permeability nature of Layer A.

Region P ranged from 890 to 830 m asl. Geologically, this portion corresponds primarily to the uppermost part of Layer B, and no significant difference in altered mineral assemblage from the lower part of Layer B was indicated. Assuming the same porosity, the mineral assemblage is considered to have no responsibility for such resistivity. Even if higher porosity is assumed, the waters in the fumarole area are not the medium that fills the pores within Region P because such waters have significantly lower resistivity than the observed resistivity. We thus assume that the resistive zone, at approximately 150 m (= 850 m asl) beneath the ECA, is a vapor pocket.

Simulation results revealed the development of an excess pressure zone at the top of the vapor-dominated hydrothermal system immediately beneath a low-permeability layer (Ingebritsen and Sorey 1988). An excess pressure zone is formed to allow heat transfer by steam moving across the low-permeability layer when conductive transfer is not sufficient for the heat input from the bottom of the hydrothermal system, and a steaming area
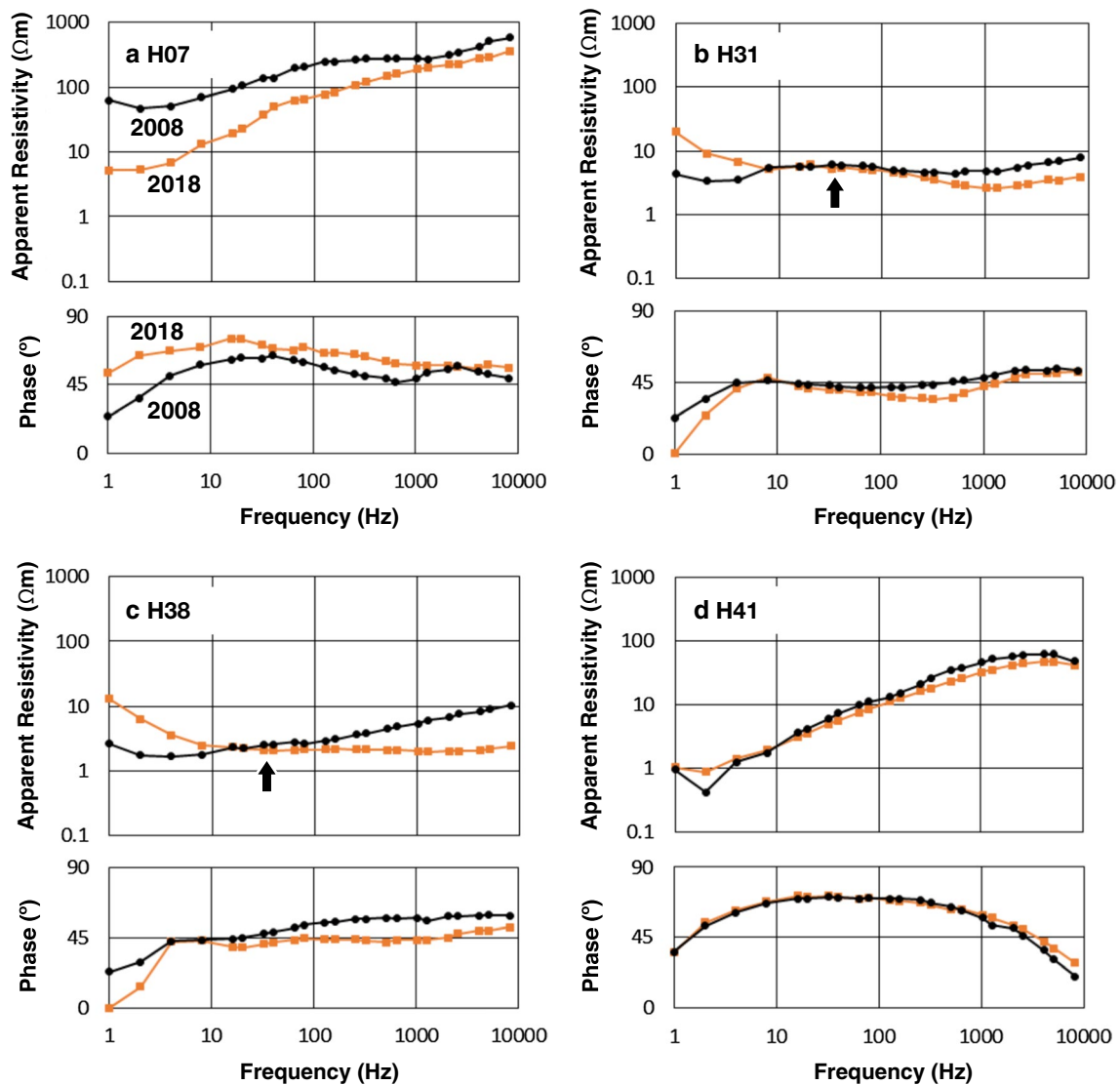
Mannen *et al. Earth, Planets and Space* (2019) 71:135

Page 15 of 20

Fig. 7 Examples of CSAMT data from 2008 (black) and 2018 (orange) surveys at four locations on survey line Fa. Apparent resistivity (upper panel) and phase angle (lower panel) data are displayed as a function of the frequency at receiver Stations H07, H31, H38, and H41. H07 represents the stations above the conductive Region U. H31 and H38 represent the stations above the resistive Region P presented in Fig. 5. A significant change can be observed between the data from 2008 to 2018 at Stations H07, H31, and H38. Conversely, no significant change can be observed at H41. The slight increase in resistivity in the range of 10–100 Hz in H31 and H38 (arrow) indicates the existence of the shallow resistive Region P

is formed at the surface immediately above the excess pressure zone (Ingebritsen and Sorey 1988).
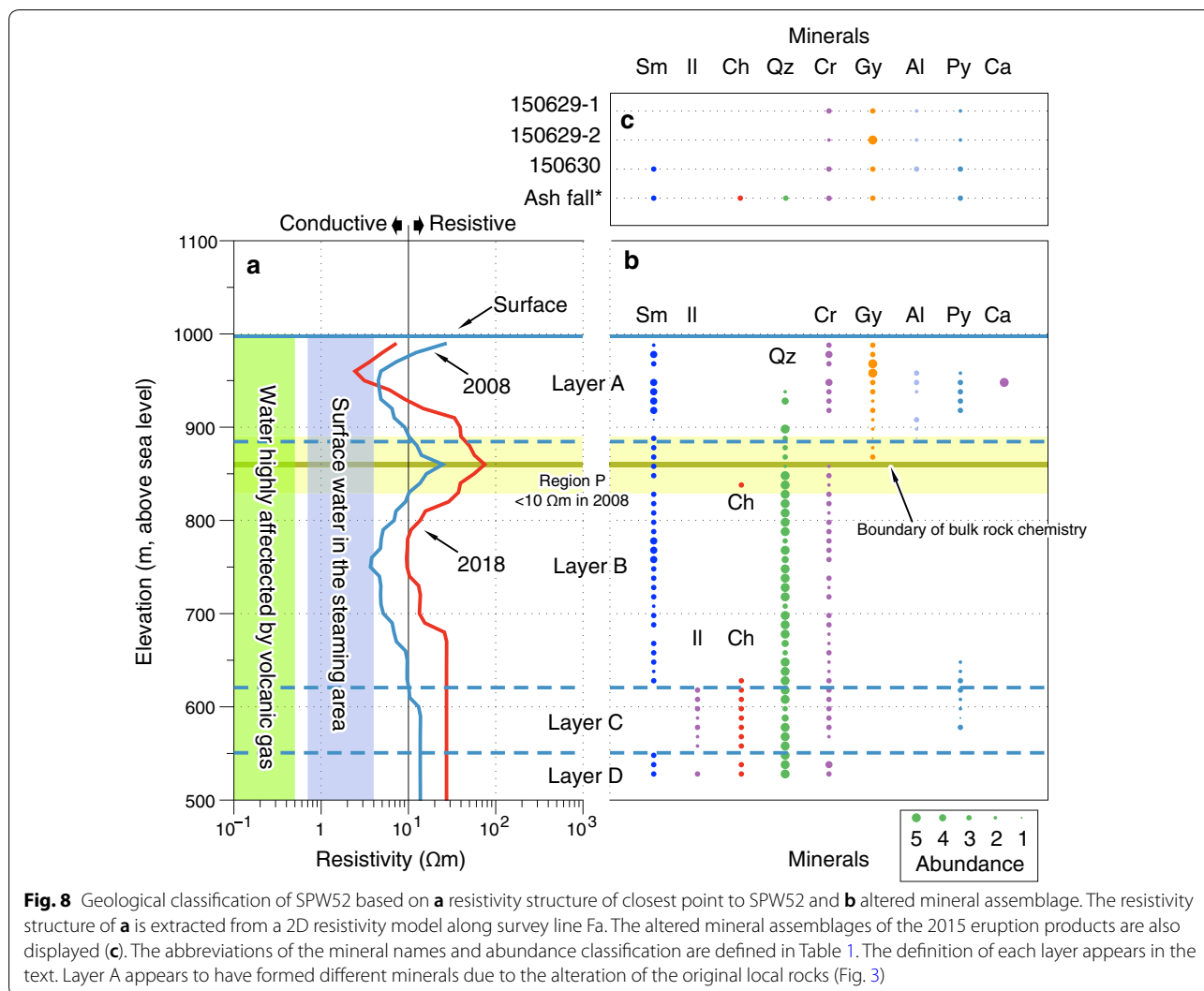
In the upper part of Region P and overlying Layer IIa, the leaching of Na and other cations was observed (> approximately 860 m asl). Such leaching could be caused by the oxidation of H_2S, which is the dominant sulfur gas of the Owakudani steaming area. The oxidation of H_2S generates SO_2, which is a strong acid, and the water with the sulfite ions dissolves the preexisting minerals. The transportation of this acidic solution, changes in temperature, and other physiochemical environmental

factors on the path to the surface could form the different minerals in Layer IIa (= Layer A).

A schematic geological model beneath the ECA based on the discussion above is summarized in Fig. 9.

Eruption source of the 2015 eruption

Because the mineral assemblage of Layer A and the 2015 eruption products were similar, it is reasonable to assume that the eruption source was not significantly deeper than the lower limit of Layer A (888 m asl). The water emitted during the 2015 eruption could support a
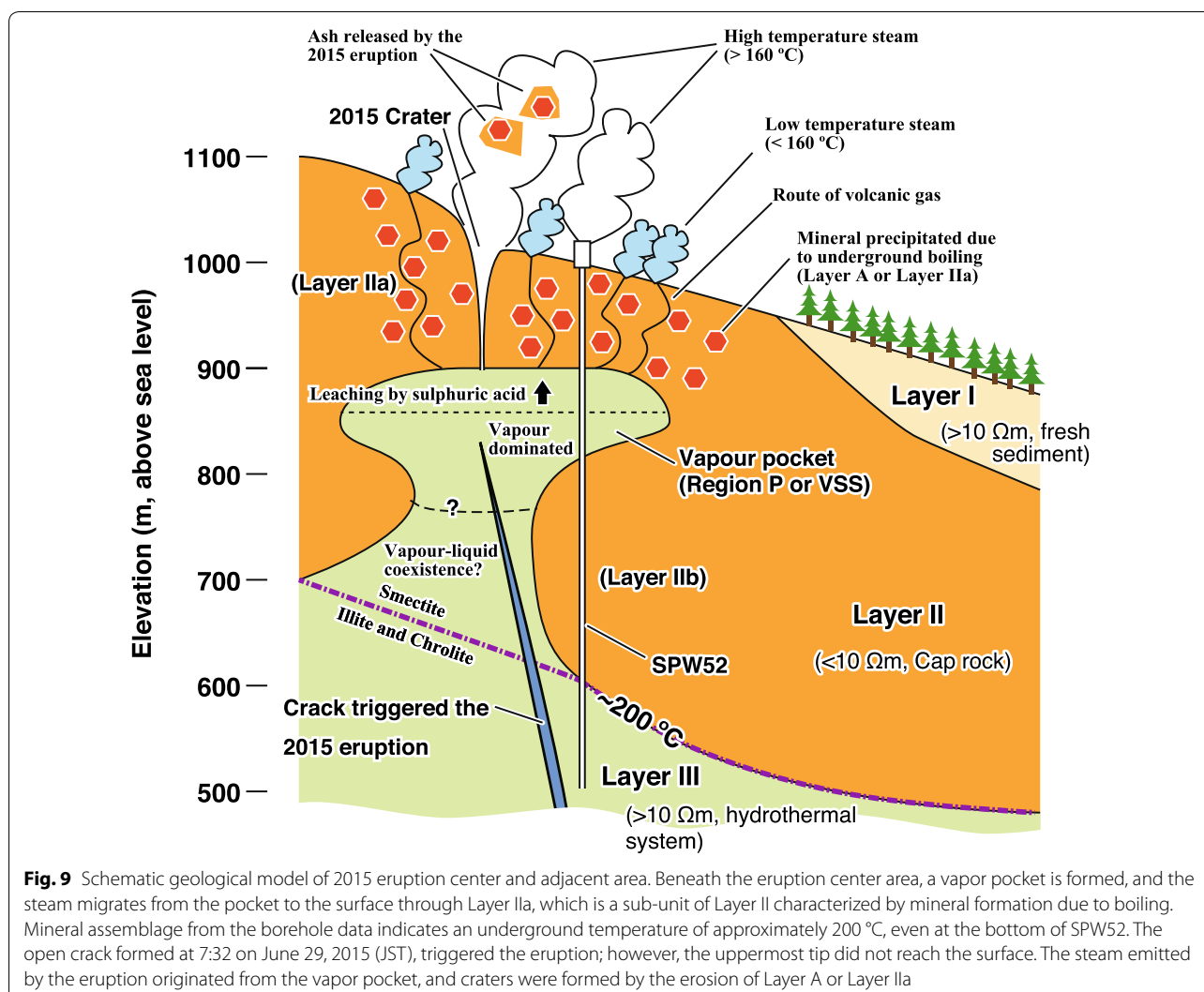
Mannen *et al. Earth, Planets and Space* (2019) 71:135

Page 16 of 20

Fig. 8 Geological classification of SPW52 based on **a** resistivity structure of closest point to SPW52 and **b** altered mineral assemblage. The resistivity structure of **a** is extracted from a 2D resistivity model along survey line Fa. The altered mineral assemblages of the 2015 eruption products are also displayed (**c**). The abbreviations of the mineral names and abundance classification are defined in Table 1. The definition of each layer appears in the text. Layer A appears to have formed different minerals due to the alteration of the original local rocks (Fig. 3)

relatively shallow eruption source. During the 2015 eruption, muddy water seemingly erupted from the craters and poured into the Owakuzawa River (Mannen et al. 2018b). The resistivity of the river water during the eruption (1.64 Ωm) was slightly less than that of the present surface waters; however, it was significantly greater than that of the waters highly influenced by the fumarole gas. Thus, we consider that the water ejected during the eruption was not geothermal fluid from deep beneath the ECA; rather, we deduce that it was surface water gently influenced by the fumaroles (Mannen et al. 2018b).

The VSS, which had been active since the early phase of the volcanic unrest (early May 2015) and then inactive after the eruption, was thought to be approximately 900–850 m asl beneath the ECA (Doke et al. 2018; Kobayashi et al. 2018). Considering these factors, it is reasonable to assume that the VSS corresponds to the vapor pocket

and that the 2015 eruption ruptured the vapor pocket. On the path from the pocket to the surface, a conduit system for steam formed, and erosion of the conduit wall by the vigorously uprising steam produced the fine particles released during the eruption (Fig. 9).

The geophysical monitoring implied that the 2015 Hakone eruption was triggered by an open crack formation with a width and topmost elevation considered to range from 1333–300 m to 854–828 m asl, respectively, by inversion analyses (Doke et al. 2018; Honda et al. 2018) (Fig. 9). However, the solid material that erupted did not originate from the depth where the open crack formed.

Such a shallow explosion source, inferred from the 2015 Hakone eruption, contrasts with the larger phreatic eruption. A comparative mineralogical study of the 2014 Ontake phreatic eruption in Japan and late-stage

Fig. 9 Schematic geological model of 2015 eruption center and adjacent area. Beneath the eruption center area, a vapor pocket is formed, and the steam migrates from the pocket to the surface through Layer IIa, which is a sub-unit of Layer II characterized by mineral formation due to boiling. Mineral assemblage from the borehole data indicates an underground temperature of approximately 200 °C, even at the bottom of SPW52. The open crack formed at 7:32 on June 29, 2015 (JST), triggered the eruption; however, the uppermost tip did not reach the surface. The steam emitted by the eruption originated from the vapor pocket, and craters were formed by the erosion of Layer A or Layer IIa

porphyry copper system concluded that the 2014 Ontake eruption contained material that originated from a depth of up to 2 km (Minami et al. 2016). The equilibrium temperature of the sulfur isotopes of native sulfur and sulfur in pyrite in the eruption products of the 2014 Ontake eruption was estimated to be 270–281 °C (Ikehata and Maruoka 2016), which also inferred a deeper source (>540 m from the steam table, assuming hydrostatic pressure) than that of the 2015 Hakone eruption.

The 2014 eruption of the Ontake volcano released tephra in the order of 10^6 m³ as air falls and surges, and dispersed ballistic ejecta that formed impact craters up to 950 m from the vent (Kaneko et al. 2016; Maeno et al. 2016; Oikawa et al. 2016; Takarada et al. 2016). These

numbers were significantly greater than those of the 2015 Hakone eruption: 100 m³ of tephra without surge and ballistic ejecta up to only 30 m from the source vent (Mannen et al. 2018b). Even though there was such a large difference in the explosiveness, the volume change of the shallow inflation source before the eruption was not significantly different in these eruptions (0.38×10^6 m³ for Ontake and 0.11–0.16×10^6 m³ for Hakone) (Takagi and Onizawa 2016; Doke et al. 2018; Honda et al. 2018). This fact could suggest that another factor, such as the geometry of the conduit, confined pressure of hydrothermal fluid, and/or phreatic environment, controls the explosiveness of phreatic eruptions. Further studies are clearly required.

Mannen *et al. Earth, Planets and Space*   (2019) 71:135

Page 18 of 20

Temporal change of the vapor pocket

We previously noted that the smectite-bearing layer detected in SPW52 corresponded to the conductive zone, the resistivity of which was less than 10 Ωm. Yoshimura et al. (2018) first proposed such a correlation, and it appears to correspond well with the 2008 survey; however, it did not effectively fit the 2018 survey. The biggest difference in the 2018 survey was a contraction of the conductive zone (Fig. 5a, c). Along SPW52, a zone of less than 10 Ωm was virtually missing below 900 m asl, and the vapor pocket appeared to inflate with higher resistivity (Fig. 8). Because our survey setting and analysis were the same in 2008 and 2018, a change in the geological environment beneath the area is thought to be the primary factor responsible for the increase in resistivity. The steaming activity notably intensified after the 2015 eruption, and inflation of the VSS was observed before the eruption without significant post-eruptive deflation. Thus, the increase in porosity and replacement of water in the pores by vapor appears to be the most probable explanation for the increase in resistivity.

Sealing zone of Hakone volcano

A phreatic eruption is a phenomenon that releases confined hydrothermal fluid to the surface in an explosive manner. As a confinement body of a hydrothermal system, a sealing zone is assumed to exist beneath the eruption center, and its rupture is considered to cause a phreatic eruption. The 2015 phreatic eruption of the Hakone volcano appears to have been triggered by the formation of an open crack 5 h before the ash emission (Doke et al. 2018; Honda et al. 2018; Mannen et al. 2018b). In this study, the rupture of the hydrothermal system and its sealing zone were clarified. The ruptured hydrothermal system was the vapor pocket located at a depth of approximately 150 m immediately beneath the ECA, and the sealing body was Layer A above the vapor pocket.

We do not deny the existence of other sealing zones in the hydrothermal system of Hakone volcano; however, they were not evident in our resistivity profiles. Ohba et al. (2011) identified an increase in the CO_2/H_2S ratio in the fumarolic gasses in the Owakudani area at the time of the volcanic unrests in 2001, 2006, and 2008, and they attributed the CO_2 increase to the rupture of the sealing zone around the degassing magma deep beneath the volcano. The earthquake swarm in Hakone volcano appears to have been triggered by the migration of highly pressured pore fluid along the preexisting fault (Yukutake et al. 2011). The origin of the pressured fluid could be hydrothermal fluid beneath the self-sealing zone formed at the boundary between the brittle–plastic transition, commonly occurring at approximately 400 °C (Fournier 1999), which is considerably greater than that of the temperature of the base of Layer II (approximately 200 °C). Doke et al. (2018) proposed that the crack formation on the morning of the eruption day was caused by a rupture of an aquitard located 300–400 m asl. Such an aquitard can be called a sealing zone.

Conclusion

Beneath the central cones of Hakone volcano, a bell-shaped conductive body exists and appears to confine the hydrothermal system of the volcano within. Our local CSAMT and geological analysis revealed that a smectite-rich layer forms the conductive body. The conductive body, however, hosts a small (< 200 m in diameter) resistive zone approximately 150 m beneath the Owakudani steaming area, which is the most active fumarole area of the volcano and was the center of the 2015 phreatic eruption. The small resistive zone, which is formed near the top of the bell-shaped conductor, can be interpreted as a vapor pocket and confined by the overlying conductive body, which is thin (approximately 100 m) and geologically characterized by a variety of altered minerals such as gypsum, alunite, and pyrite. These altered minerals are considered to have been formed by boiling and associated processes. The formation of these altered minerals within the veins and pores is considered to have made the conductive body impermeable. Thus, we postulated that the thin surface conductive body functioned as the major sealing zone that separated the surface aquifer and vapor pocket. The 2015 eruption was triggered by an intrusion of hydrothermal fluid that occurred at depth (< 854 m asl). However, our analysis of the erupted material revealed that only material from shallow depths (> 900 m asl) was delivered to the surface. The water of the mudflow retrieved during the eruption also indicated an extremely limited contribution of hydrothermal water; the majority of the erupted water should have originated from shallow groundwater (Mannen et al. 2018b). We inferred from our analysis that the rupture of a shallow sealing zone, triggered by deep intrusion, was the nature of the 2015 Hakone eruption. Because the 2014 Ontake eruption, which was considerably more destructive than the 2015 Hakone eruption, emitted material from deep beneath the volcano (< 2 km), rupture development at depth could be a key factor in determining the explosiveness of a phreatic eruption.

Mannen *et al. Earth, Planets and Space*   (2019) 71:135

Page 19 of 20

Supplementary information

Supplementary information accompanies this paper at https://doi.org/10.1186/s40623-019-1116-5.

Additional file 1. Temperature, pH, conductivity and major cation and anion contents of waters in Owakudani.

Additional file 2. Cross-sectional resistivity structure along survey lines of this study. The 2018, 2008 and resistivity change in log (R2018–R2008) are shown.

Abbreviations

CSAMT: controlled source audio frequency magnetotellurics; ECA: eruption center area of the 2015 Hakone eruption; InSAR: Interferometric Synthetic Aperture Radar; JST: Japan Standard Time; SPW: steam production well; UTC: Universal Time Coordinated; VSS: very shallow source of inflation beneath ECA detected by satellite InSAR analysis.

Authors' contributions

KM compiled the data and drafted the manuscript. TT planned the 2008 and 2018 surveys. AJ and TA performed the CSAMT survey and related analysis. GK performed analysis of water chemistry. YF and FK performed a geological survey of the borehole. HY performed XRF analysis. All authors read and approved the final manuscript.

Availability of data and materials

The datasets used and/or analyzed during the current study are available from the corresponding author upon reasonable request.

Competing interests

The authors declare that they have no competing interests.

Author details

[1] Hot Springs Research Institute of Kanagawa Prefecture, 586 Iriuda, Odawara, Kanagawa 250-0031, Japan. [2] National Research Institute for Earth Science and Disaster Resilience, 3-1 Tennodai, Tsukuba, Ibaraki 305-0006, Japan. [3] Neo Science Co. Ltd., 4-2-30, Tarui, Sennan, Osaka 590-0521, Japan. [4] Geothermal Engineering Co. Ltd., 356-6 Oshimizu, Ogama, Takizawa, Iwate 020-0758, Japan. [5] Tokyo Gakugei University, 4-1-1 Nukui Kita, Koganei, Tokyo 184-8501, Japan. [6] Kanagawa Prefectural Museum of Natural History, 499 Iriuda, Odawara, Kanagawa 250-0031, Japan.

References

Aizawa K, Ogawa Y, Mishina M, Takahashi K, Nagaoka S, Takagi N, Sakanaka S, Miura T (2009) Structural controls on the 1998 volcanic unrest at Iwate volcano: relationship between a shallow, electrically resistive body and the possible ascent route of magmatic fluid. J Volcanol Geotherm Res 187:131–139. https://doi.org/10.1016/j.jvolgeores.2009.08.009

Doke R, Harada M, Mannen K, Itadera K, Takenaka J (2018) InSAR analysis for detecting the route of hydrothermal fluid to the surface during the 2015 phreatic eruption of Hakone Volcano. Earth Planets Space, Japan. https://doi.org/10.1186/s40623-018-0834-4

Fournier RO (1999) Hydrothermal processes related to movement of fluid from plastic into brittle rock in the magmatic-epithermal environment. Econ Geol 94:1193–1211. https://doi.org/10.2113/gsecongeo.94.8.1193

Goto Y, Johmori A (2013) Resistivity Structure of the Hiyoriyama Cryptodome at Kuttara Volcano, Hokkaido, Japan. Bull Volcanol Soc Japan 58:2013

Harada M, Odawara K, Matsuzawa S, Daita Y, Itadera K, Tanada K (2012) Changes of surface conditions and infrared thermal camera observation at the northern side of Owakudani, Hakone volcano. Bull Hot Springs Res Inst Kanagawa Prefect 44:55–62 **(in Japanese with English abstract)**

Harada M, Doke R, Mannen K, Itadera K, Satomura M (2018) Temporal changes in inflation sources during the 2015 unrest and eruption of Hakone volcano, Japan. Earth Planets Space 70:152. https://doi.org/10.1186/s40623-018-0923-4

Hedenquist JW, Arribas RA, Gonzalez-Urien E (2000) Chapter 7 exploration for epithermal gold deposits. SEG Rev 13:245–277

Henley RW, Ellis AJ (1983) Geothermal systems ancient and modern: a geochemical review. Earth Sci Rev 19:1–50. https://doi.org/10.1016/0012-8252(83)90075-2

Hogg C, Kiyan D, Rath V, Byrdina S, Vandemeulebrouck J, Revil A, Viveiros F, Carmo R, Silva C, Ferreira T (2018) 3-D interpretation of short-period magnetotelluric data at Furnas Volcano, Azores Islands. Geophys J Int 213:371–386. https://doi.org/10.1093/gji/ggx512

Honda R, Yukutake Y, Morita Y, Sakai S, Itadera K, Kokubo K (2018) Precursory tilt changes associated with a phreatic eruption of the Hakone volcano and the corresponding source model. Earth Planets Space. https://doi.org/10.1186/s40623-018-0887-4

Ikehata K, Maruoka T (2016) Sulfur isotopic characteristics of volcanic products from the September 2014 Mount Ontake eruption. Earth Planets Space, Japan. https://doi.org/10.1186/s40623-016-0496-z

Ingebritsen SE, Sorey ML (1988) Vapor-dominated zones within hydrothermal systems: evolution and natural state. J Geophys Res 93655:635. https://doi.org/10.1029/JB093iB11p13635

Inoue A (1995) Formation of clay minerals in hydrothermal environments. In: Velde B (ed) Origin and mineralogy of clays. Springer, Berlin, pp 268–329

Johmori A, Mitsuhata Y, Nishimura S, Johmori N, Kondou T, Takahashi T (2010) Development of a deep electoromagnetic exploration instrument with high frequency spectrum resolution using GPS synchronization. J Jap Soc Eng Geol 51:62–72 **(in Japanese with English abstract)**

Kaneko T, Maeno F, Nakada S (2016) 2014 Mount Ontake eruption: characteristics of the phreatic eruption as inferred from aerial observations. Earth Planets Space 68:72. https://doi.org/10.1186/s40623-016-0452-y

Kobayashi T, Morishita Y, Munekane H (2018) First detection of precursory ground inflation of a small phreatic eruption by InSAR. Earth Planet Sci Lett 491:244–254. https://doi.org/10.1016/j.epsl.2018.03.041

Kuraoka S, Nakashima Y, Doke R, Mannen K (2018) Monitoring ground deformation of eruption center by ground—based interferometric synthetic aperture radar (GB-InSAR): a case study during the 2015 phreatic eruption of Hakone volcano. Earth Planets Space. https://doi.org/10.1186/s40623-018-0951-0

Lee JO, Kang IM, Cho WJ (2010) Smectite alteration and its influence on the barrier properties of smectite clay for a repository. Appl Clay Sci 47:99–104. https://doi.org/10.1016/j.clay.2008.10.007

Maeno F, Nakada S, Oikawa T, Yoshimoto M, Komori J, Ishizuka Y, Takeshita Y, Shimano T, Kaneko T, Nagai M (2016) Reconstruction of a phreatic eruption on 27 September 2014 at Ontake volcano, central Japan, based on proximal pyroclastic density current and fallout deposits the Phreatic Eruption of Mt. Ontake Volcano in 2014. 5. Volcanology. Earth Planets Space. https://doi.org/10.1186/s40623-016-0449-6

Mannen K, Kikugawa G, Miyashita Y, Yamaguchi T, Tanbo T, Honma N (2018a) Steaming area formed after the 2015 eruption of Hakone volcano, Japan and sequential changes of fumarolic temperature. Bull Hot Springs Res Inst Kanagawa Prefect 50:19–44 **(in Japanese with English abstract)**

Mannen K, Yukutake Y, Kikugawa G, Harada M, Itadera K, Takenaka J (2018b) Chronology of the 2015 eruption of Hakone volcano, Japan—geological background, mechanism of volcanic unrest and disaster mitigation

measures during the crisis. Earth Planets Space 70:68. https://doi.org/10.1186/s40623-018-0844-2

Mannen K, Roman D, Leonard G, Prejean S, Nakagawa M (2019) Special issue "Towards forecasting phreatic eruptions: examples from Hakone volcano and some global equivalents". Earth Planets Space 71:1–6. https://doi.org/10.1186/s40623-019-1068-9

Minami Y, Imura T, Hayashi S, Ohba T (2016) Mineralogical study on volcanic ash of the eruption on September 27, 2014 at Ontake volcano, central Japan: correlation with porphyry copper systems. Earth Planets Space. https://doi.org/10.1186/s40623-016-0440-2

Ohba T, Daita Y, Sawa T, Taira N, Kakuage Y (2011) Coseismic changes in the chemical composition of volcanic gases from the Owakudani geothermal area on Hakone volcano, Japan. Bull Volcanol 73:457–469. https://doi.org/10.1007/s00445-010-0445-9

Oikawa T, Yoshimoto M, Nakada S, Maeno F, Komori J, Shimano T, Takeshita Y, Ishizuka Y, Ishimine Y (2016) Reconstruction of the 2014 eruption sequence of Ontake Volcano from recorded images and interviews. Earth Planets Space 68:79. https://doi.org/10.1186/s40623-016-0458-5

Sandberg SK, Hohmann GW (1982) Controlled-source audiomagnetotellurics in geothermal exploration. Geophysics 47:100–116. https://doi.org/10.1190/1.1441272

Sasaki Y (1986) Resolving power of MT method for two-dimensional structures. Butsuri-tansa (Geophysical Exploration) 39:207–215 **(in Japanese with English abstract)**

Seki K, Kanda W, Ogawa Y, Tanbo T, Kobayashi T, Hino Y, Hase H (2015) Imaging the hydrothermal system beneath the Jigokudani valley, Tateyama volcano, Japan: implications for structures controlling repeated phreatic eruptions from an audio-frequency magnetotelluric survey. Earth Planets Space 67:6. https://doi.org/10.1186/s40623-014-0169-8

Seki K, Kanda W, Tanbo T, Ohba T, Ogawa Y, Takakura S, Nogami K, Ushioda M, Suzuki A, Saito Z, Matsunaga Y (2016) Resistivity structure and geochemistry of the Jigokudani Valley hydrothermal system, Mt. Tateyama, Japan. J Volcanol Geotherm Res 325:15–26. https://doi.org/10.1016/j.jvolgeores.2016.06.010

Stix J, De Moor MJ (2018) Understanding and forecasting phreatic eruptions driven by magmatic degassing. Earth Planets Space. https://doi.org/10.1186/s40623-018-0855-z

Takagi A, Onizawa S (2016) Shallow pressure sources associated with the 2007 and 2014 phreatic eruptions of Mt. Ontake, Japan. Earth Planets Space 68:135. https://doi.org/10.1186/s40623-016-0515-0

Takarada S, Oikawa T, Furukawa R, Hoshizumi H, Itoh J, Geshi N, Miyagi I (2016) Estimation of total discharged mass from the phreatic eruption of Ontake Volcano, central Japan, on September 27, 2014. Earth Planets Space 68:1–9. https://doi.org/10.1186/s40623-016-0511-4

The Geological Society of Japan (2007) Hakone Volcano. Geological Society of Japan

Weatherley DK, Henley RW (2013) Flash vaporization during earthquakes evidenced by gold deposits. Nat Geosci 6:294–298. https://doi.org/10.1038/ngeo1759

Yaguchi M, Ohba T, Sago M (2019) The nature and source of the volcanic ash during the 2015 small phreatic eruption at Hakone volcano, central Japan. Geochem J 53:209–217. https://doi.org/10.2343/geochemj.2.0560

Yamaoka K, Geshi N, Hashimoto T, Ingebritsen SE, Oikawa T (2016) Special issue "the phreatic eruption of Mt. Ontake volcano in 2014" the Phreatic Eruption of Mt. Ontake Volcano in 2014. 5. Volcanology. Earth Planets Space. https://doi.org/10.1186/s40623-016-0548-4

Yoshimura R, Ogawa Y, Yukutake Y, Kanda W, Komori S, Hase H, Goto T, Honda R, Harada M, Yamazaki T, Kamo M, Kawasaki S, Higa T, Suzuki T, Yasuda Y, Tani M, Usui Y (2018) Resistivity characterisation of Hakone volcano, Central Japan, by three-dimensional magnetotelluric inversion. Earth Planets Space 70:66. https://doi.org/10.1186/s40623-018-0848-y

Yukutake Y, Ito H, Honda R, Harada M, Tanada K, Yoshida A (2011) Fluid-induced swarm earthquake sequence revealed by precisely determined hypocenters and focal mechanisms in the 2009 activity at Hakone volcano, Japan. J Geophys Res Solid Earth 116:1–13. https://doi.org/10.1029/2010JB008036

Yukutake Y, Honda R, Harada M, Doke R, Saito T, Ueno T, Sakai S, Morita Y (2017) Continuous volcanic tremor during the 2015 phreatic eruption in Hakone volcano. Earth Planets Space. https://doi.org/10.1186/s40623-017-0751-y

Yukutake Y, Ichihara M, Honda R (2018) Infrasonic wave accompanying a crack opening during the 2015 Hakone eruption. Earth Planets Space. https://doi.org/10.1186/s40623-018-0820-x

Zonge KL, Hughes LJ (1991) Controlled source audio-frequency magnetotellurics. In: Nabighian MN (ed) Investigations in Geophysics No. 3 Electromagnetic Methods in Applied Geophysics Part A and B, 2nd printi. Society of Exploration Geophysicists, Tulsa, pp 713–809

Publisher's Note